ACS Catalysis

Letter

pubs.acs.org/acscatalysis

Iridium Complexes and Clusters in Dealuminated Zeolite HY: Distribution between Crystalline and Impurity Amorphous Regions

Claudia Martinez-Macias,[†] Pinghong Xu,[†] Son-Jong Hwang,[⊥] Jing Lu,[†] Cong-Yan Chen,[†,§] Nigel D. Browning,[‡] and Bruce C. Gates*[,†]

[†]Department of Chemical Engineering and Materials Science, University of California at Davis, Davis, California 95616, United States

[‡]Fundamental and Computational Sciences, Pacific Northwest National Laboratory, Richland, Washington 99352, United States

[§]Chevron Energy Technology Co., Richmond, California 94708, United States

[⊥]Division of Chemistry and Chemical Engineering, California Institute of Technology, Pasadena, California 91125, United States

Supporting Information

ABSTRACT: Dealuminated zeolite HY was used to support $Ir(CO)_2$ complexes formed from $Ir(CO)_2(C_5H_7O_2)$. Infrared and X-ray absorption spectra and atomic resolution electron microscopy images identify these complexes, and the images and ^{27}Al NMR spectra identify impurity amorphous regions in the zeolite where the iridium is more susceptible to aggregation than in the crystalline regions. The results indicate the value of electron microscopy in characterizing the amorphous impurity regions of zeolites and a significant stability limitation of metals in these regions of zeolite catalyst supports.

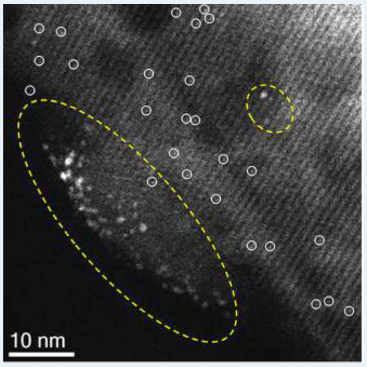

KEYWORDS: *iridium, zeolite, scanning transmission electron microscopy, amorphous region of zeolite, supported metal catalyst*

Zeolites that incorporate highly dispersed platinum and palladium are widely used as catalysts, finding applications for hydrocracking,[1] hydroisomerization,[2] and dehydrocyclization.[3] The metals in these catalysts are highly dispersed, some present in clusters of only a few metal atoms each.[4] The catalytic properties depend on the cluster size and cluster–support interactions. Zeolites are among the few crystalline materials that find industrial catalytic applications, but they often incorporate amorphous material that is formed, for example, in dealumination processes.[5] Only little is known about the amorphous material in zeolites, and there is no information characterizing the distributions of supported metals between the amorphous and crystalline regions.

Here, we present microscopic and spectroscopic evidence characterizing both of these regions in dealuminated zeolite HY and highly dispersed iridium in them. The results demonstrate that the metal is preferentially present in the amorphous regions and more susceptible to sintering there than in the crystalline regions. Dealuminated HY zeolite was chosen as the support because it is widely applied in catalytic technology, and iridium was chosen as the metal because it is comparable to the commonly applied platinum in industrial catalysts and can be incorporated in the support in well-defined structures formed by the reaction of the support surface with $Ir(CO)_2(acac)$ (acac is acetylacetonate, $C_5H_7O_2$) to give anchored $Ir(CO)_2$ complexes, which lend themselves to incisive characterization.

Infrared (IR) spectra (Figure 1) show that reaction of $Ir(CO)_2(acac)$ with the support led to a decrease in intensity of ~40% of the 3630 cm^{-1} band that is assigned to isolated

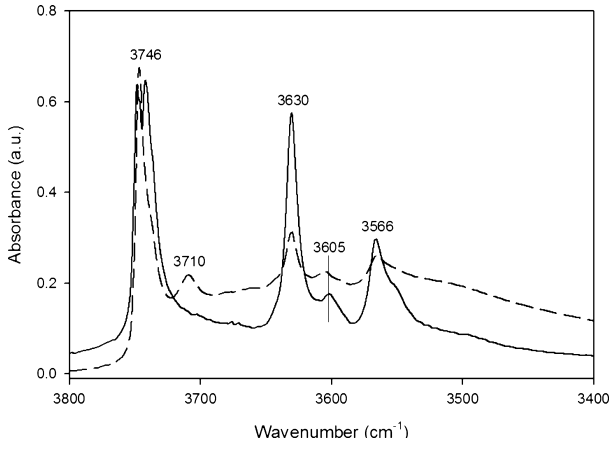

Figure 1. IR spectra characterizing the bare dealuminated HY zeolite (solid line) and the zeolite after reaction with $Ir(CO)_2(acac)$ (dashed line).

Received: May 9, 2014
Revised: June 29, 2014
Published: July 8, 2014

hydroxyl groups bonded at Al sites in the zeolite supercages.[6,7] The results thus demonstrate that the cationic iridium complexes were bonded where there had been acidic sites in the supercages (the acac ligands were largely converted to Hacac).[8] The ν_{CO} IR bands characterizing the initially formed sample (Supporting Information (SI), Figures S1 and S2), at 2109 and 2038 cm^{-1}, demonstrate the presence of the expected mononuclear iridium *gem*-dicarbonyls.[9,10] The sharpness of these bands (full width at half-maximum <6 cm^{-1}) indicates highly uniform supported species.[11,12] After exposure to a CO pulse, a new band appeared at 2074 cm^{-1} while the bands at 2109 and 2038 cm^{-1} remained essentially unchanged (SI Figure S2); the new band indicates a supported iridium tricarbonyl.[10−13] There were no discernible peaks indicating bridging carbonyls, as would be expected if iridium clusters had been present in significant amounts (Table 1).

Table 1. Vibrational Frequencies of Bands Characterizing Dealuminated HY Zeolite Incorporating Iridium Carbonyls

IR band frequency (cm^{-1})	assignment	ref.
3746[a]	OH bonded to Si	7
3710[a]	OH groups associated with extraframework Al	6
3630[a]	OH bonded to Al in supercage	7
3605[a]	OH groups associated with extraframework Al	14
3566[a]	OH bonded to Al in sodalite cage	7
2109[a]	CO in $Ir(CO)_2$, symmetric mode	10
2074[b]	CO in $Ir(CO)_3$	10, 13
2038[a]	CO in $Ir(CO)_2$, antisymetric mode	10

[a]Sample in flowing helium. [b]After a CO pulse in flowing helium.

Extended X-ray absorption fine structure (EXAFS) spectra at the Ir L_{III} edge confirm the IR spectra showing that the predominant supported species present initially was mononuclear iridium complexes, with each Ir atom bonded on average (and within error) to two CO ligands and two support oxygen atoms (Table 2). There was no detectable Ir−Ir contribution, hence no EXAFS evidence of iridium clusters, again consistent with the IR spectra.

The IR spectra of the bare dealuminated zeolite include a band at 3605 cm^{-1} indicative of OH groups associated with Al sites in extraframework material,[14,15] but another such band (at 3710 cm^{-1}) was missing after calcination (SI Figure S3) leading to a high degree of dehydroxylation. However, incorporation of $Ir(CO)_2$ groups by reaction of $Ir(CO)_2(acac)$ with zeolite OH groups located at Al sites is inferred to have liberated protons that migrated to the amorphous regions to form OH groups, causing the appearance of the 3710 cm^{-1} band.[16]

Table 2. EXAFS Fit Parameters[b] Characterizing $Ir(CO)_2$ Bonded to Dealuminated HY Zeolite[a]

shell	N	R (Å)	$10^3 \times \Delta\sigma^2$ (Å^2)	ΔE_0 (eV)
$Ir-O_{zeolite}$	2.2	2.07	9.3	1.6
$Ir-C_{CO}$	1.9	1.85	10.6	6.8
$Ir-O_{CO}$	1.9	2.96	9.5	−4.9
$Ir-Al_{zeolite}$	0.9	2.99	0.8	−7.1
$Ir-Si_{zeolite}$	2.8	3.47	10.7	−7.5

[a]Data collected at 300 K and 1 bar, sample in flowing helium. [b]Notation: N, coordination number; R, distance between absorber and backscatterer atoms; $\Delta\sigma^2$, disorder term; ΔE_0, inner potential correction. Estimated error bounds: N, ±20%; R, ±0.02 Å; $\Delta\sigma^2$, ±20%; ΔE_0, ±20% (errors characterizing the $Ir-Al_{zeolite}$ and $Ir-Si_{zeolite}$ contribution are greater than these).

Dealuminated HY zeolite contains both tetrahedral Al in the crystalline framework (denoted AlO_4) and octahedral Al in nonframework regions (AlO_6).[17,18] The ^{27}Al magic angle spinning (MAS) NMR spectrum of the iridium-containing dealuminated HY zeolite (Figure 2) confirms the presence of aluminum in both framework and extraframework regions. The molar AlO_4/AlO_6 ratio determined by the ^{27}Al NMR data is 4.1:1.

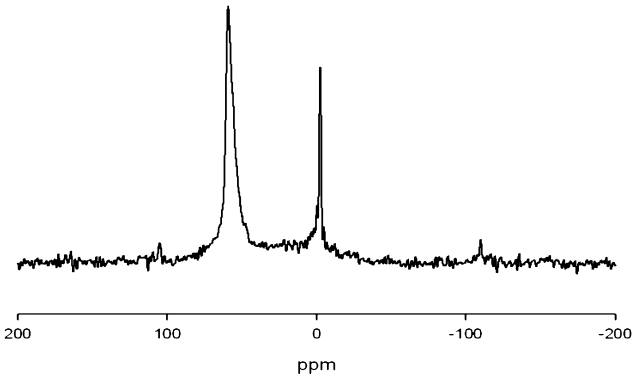

Figure 2. ^{27}Al MAS NMR spectrum of the dealuminated HY zeolite incorporating iridium carbonyl complexes formed by reaction of the zeolite with $Ir(CO)_2(acac)$.

The ^{29}Si MAS NMR (Bloch decay) spectrum of the sample (SI Figure S4A) includes peaks at −107.8[19] and −102 ppm, the former attributed to tetrahedral Si bonded to 4 SiO, denoted $Q_4(Si(OSi)_4)$, and the latter attributed to a combination of tetrahedral Si bonded to (a) 1 AlO and 3 SiO, denoted $Q_4(Si(OAl)(OSi)_3)$, and (b) terminal OH groups at outer surface and internal defect sites, denoted $Q_3(HOSi(OSi)_3)$. Data analysis focused on the −102 ppm peak indicates that $Q_3/(Q_4 + Q_3) \sim 0.05$ (details in SI).

However, the sharpness of the overall spectral lines of the MAS spectrum stymies an attempt to infer the relative distribution of the Q_3 species between the crystalline framework and the nonframework regions. Thus, we made ^{29}Si CPMAS NMR measurements (SI Figure S4B); the broadness of the peak at −102 ppm suggests not only the presence of $Q_3(\equiv HOSi(OSi)_3)$ and $Q_4(Si(OAl)(OSi)_3)$ but also amorphous regions in the material. However, the ^{27}Al MAS, ^{29}Si MAS, and ^{29}Si CPMAS NMR data are not sufficient to determine the relative distribution of the AlO_6 and Q_3 species or the fractions of the material that are amorphous and crystalline.

To pursue such information and the iridium distribution in the separate regions, we turned to high-angle annular dark-field aberration-corrected scanning transmission electron microscopy (HAADF-STEM). The images (Figure 3 and SI Figure S5) demonstrate the presence of (a) isolated Ir atoms, confirming the IR and EXAFS data indicating mononuclear iridium complexes, and (b) both crystalline and amorphous regions. Image analysis indicates that an estimated 14% of the material prior to incorporation of iridium was amorphous, but the estimate is rough because it was difficult to distinguish crystalline and amorphous regions that were not completely

dx.doi.org/10.1021/cs5006426 | ACS Catal. 2014, 4, 2662−2666

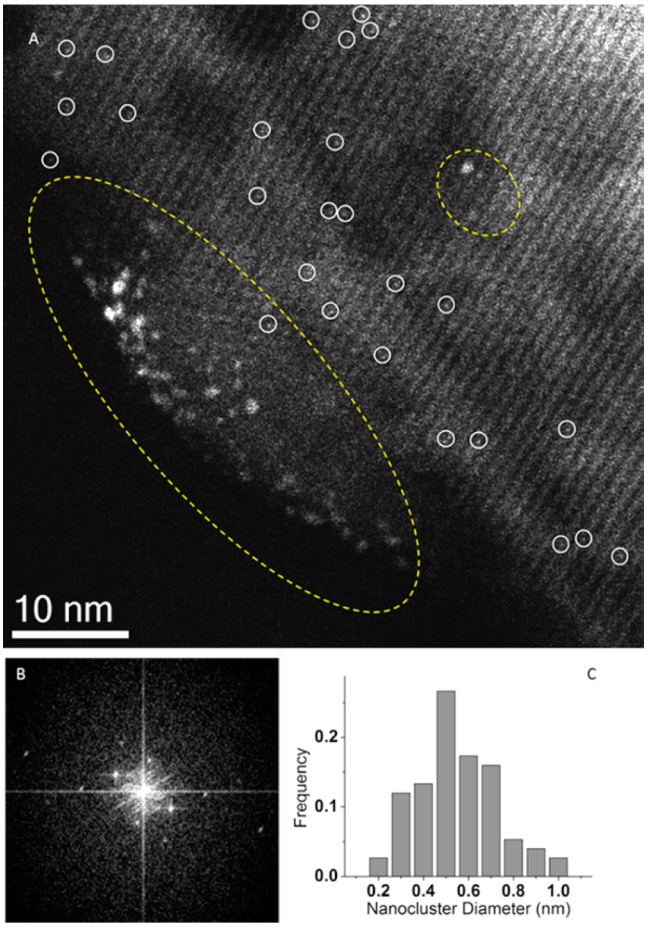

Figure 3. (A) Aberration-corrected HAADF-STEM image of dealuminated HY zeolite containing $Ir(CO)_2$ (1 wt % iridium) showing the zeolite framework in the [110] direction. Bright features in white circles are examples of site-isolated mononuclear iridium complexes in the zeolite framework; those in yellow circles are iridium clusters in amorphous regions. (B) Fast Fourier transform of the image in part A. (C) Histogram showing size distribution of iridium clusters.

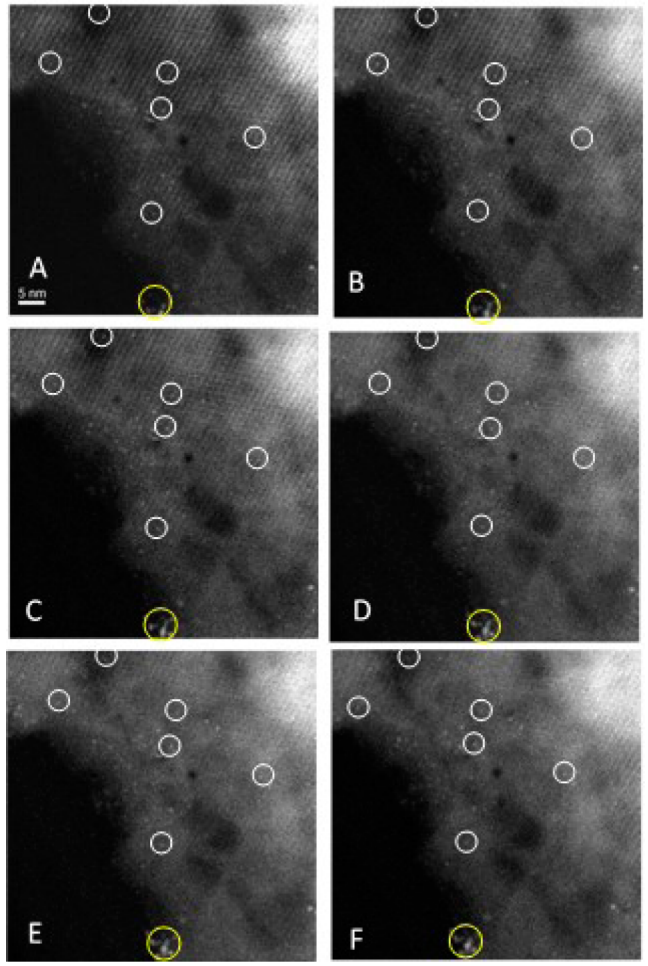

Figure 4. Sequence of HAADF-STEM images of iridium-containing dealuminated HY zeolite after the following beam exposure times (s): A, 0; B, 12; C, 24; D, 36; E, 6; F, 86. Site-isolated mononuclear iridium complexes are encircled in white and iridium clusters in yellow.

separated. Furthermore, this value may be an overestimate because of the uncertainty associated with the appearance of regions that seem to be amorphous only because of defocus issues.

The image of Figure 3A shows that iridium was present in both crystalline and amorphous regions, and qualitative image analysis showed that the iridium content of the amorphous regions was greater than that of the crystalline regions. Some of the iridium in the amorphous regions was present as clusters and not just mononuclear complexes, whereas essentially all the iridium in the crystalline regions was atomically dispersed (EXAFS and IR spectroscopy lack the sensitivity to detect these clusters). As shown in Figure 3C, the clusters in the amorphous regions had various sizes, with the mean cluster diameter being 0.60 ± 0.18 nm, corresponding to only several Ir atoms per cluster.[20] The error bound represents the standard deviation in measurements of 75 clusters in the images (Figure 3 and SI Figure S6).

STEM images of this iridium-containing zeolite recorded after various times of exposure to the electron beam (Figure 4) show that the beam caused aggregation of the iridium and that the aggregation took place more readily in the amorphous than the crystalline regions. Data characterizing supported iridium species similar to ours[21] demonstrate a parallel between the aggregation occurring under the influence of the electron beam and that occurring in the presence of H_2. Thus, we infer that metals such as iridium (and, by extension, other platinum-group metals) in the amorphous regions of practical zeolite catalysts will be less stably dispersed than metals in the crystalline regions.

To provide a comparison with the amorphous regions of the zeolite, we investigated samples with porous (amorphous) γ-Al_2O_3 as a support using the same synthesis procedure mentioned above. Again, the IR spectra show $Ir(CO)_2$ without evidence of bridging carbonyls (SI Figure S7), hence, mononuclear iridium species. However, the STEM images demonstrate the presence of some small iridium clusters along with atomically dispersed iridium, as in the amorphous regions of the zeolite (SI Figure S8). Thus, the data show that the crystalline region of the zeolite, with its small, confining pores, stabilizes mononuclear metal complexes more effectively than amorphous materials because, we infer,[22] the zeolite cage walls limit the migration of the metal to form clusters, and this channel confinement is limited to the crystalline regions because of the smaller pores in those regions.

In summary, our results provide the first microscopic evidence of amorphous regions in a zeolite and the first

dx.doi.org/10.1021/cs5006426 | ACS Catal. 2014, 4, 2662−2666

evidence of the distribution and state of metal dispersed separately in the amorphous and crystalline regions. The results demonstrate the advantages of STEM for characterizing these regions and the metals in them. Because zeolite-supported noble metal catalysts are industrially important and because their deactivation by metal sintering is especially fast in amorphous regions, we recognize a significant disadvantage of extraframework material in zeolite catalyst supports.

EXPERIMENTAL METHODS

$Ir(CO)_2$/HY Zeolite Synthesis. Dealuminated zeolite HY (Zeolyst International, CBV760, Si/Al atomic ratio ≅ 30, according to the manufacturer, and 27.4, as determined by inductively coupled plasma analysis at Galbraith Laboratories, Knoxville, TN, USA) was calcined in O_2 at 773 K for 2 h, followed by evacuation at 773 K for 14 h. Aluminum oxide (Aeroxide Alu C, 100 ± 15 m^2/g as stated by the manufacturer) was made into a paste by adding deionized water, followed by drying at 393 K overnight. It was ground and then calcined by the procedure mentioned above. After calcination, the support was stored in an argon-filled glovebox. The precursor ($Ir(CO)_2(acac)$, 99%, Strem) and the calcined zeolite were combined into a slurry with dried and deoxygenated *n*-pentane (Fisher, 99%) and stirred for 24 h. The solvent was then removed by evacuation for a day. The resultant powder, containing 1 wt % iridium, was stored in the glovebox.

Infrared Spectroscopy. IR spectra were recorded with a Bruker IFS 66v/S spectrometer; the spectral resolution was 2 cm^{-1}. Each sample (~30 mg) was pressed into a thin wafer and loaded between two KBr windows in a cell in the argon-filled glovebox. The cell was sealed, transferred, and connected to a flow system that allowed recording of spectra while flowing gases passed around and through the sample. The spectra were recorded with exclusion of air and moisture, at room temperature, and in flowing helium. Each spectrum represents an average of 64 scans.

MAS NMR Spectroscopy. ^{27}Al and ^{29}Si MAS NMR spectra were obtained with a Bruker DSX-500 spectrometer (11.7 T) and a 4 mm Bruker MAS probe. Approximately 70 mg of the as-prepared iridium-containing zeolite powder was packed into a zirconia rotor, and the rotor was spun at 14 kHz at room temperature. A 0.5 μs $\pi/18$ pulse for the ^{27}Al channel was employed, and a strong ^{1}H decoupling pulse was applied during signal detection; the recycle delay time was 2.0 s. The spectrum was referenced externally to a 1 *N* solution of aqueous $Al(NO_3)_3$. ^{29}Si MAS NMR spectra were recorded at a 8 kHz spinning rate with a 4 μs $\pi/2$ pulse, followed by a strong ^{1}H decoupling pulse and a recycle delay time of 60 s. ^{29}Si CPMAS NMR spectra were obtained at 8 kHz with a 2.0 ms CP contact time. ^{29}Si NMR spectra were referenced to tetramethylsilane.

STEM Imaging and Sample Handling. STEM samples were prepared by dipping a 200-mesh lacey-carbon-coated cooper grid (Ted-Pella) into the initially prepared catalyst powder in the glovebox. Samples were transported to the microscope and mounted onto a sample holder in an argon-filled glovebag, and transferred to the microscope with a period of air exposure of <3 s. Samples were imaged with an aberration-corrected FEI Titan 80/300S operating at 300 keV; the convergence angle was 35.6 mrad; the HAADF collection inner angle was ~75 mrad. To minimize artifacts in the images caused by beam damage, the microscope was aligned for one region of the sample, and then the beam was shifted to a neighboring region for quick image acquisition.

ASSOCIATED CONTENT

Supporting Information

Experimental details, additional spectra, and images. This material is available free of charge via the Internet at http://pubs.acs.org.

AUTHOR INFORMATION

Corresponding Author

*E-mail: bcgates@ucdavis.edu.

Notes

The authors declare no competing financial interest.

ACKNOWLEDGMENTS

This work was supported by the U.S. Department of Energy (DOE), Office of Science, Basic Energy Sciences, Grants DE-FG02-04ER15513 (C.M.M.) and DE-FG02-03ER46057 (P.X.) through the University of California, Davis; the Laboratory Directed Research and Development Program: Chemical Imaging Initiative, at Pacific Northwest National Laboratory (PNNL); and the Environmental Molecular Sciences Laboratory, a national scientific user facility sponsored by the DOE's Office of Biological and Environmental Research and located at PNNL, a multiprogram national laboratory operated by Battelle for DOE under Contract DE-AC05-76RL01830. C.M.M. was supported in part by the UC MEXUS-CONACYT doctoral fellowship program. Use of the Advanced Photon Source, an Office of Science User Facility operated for DOE by Argonne National Laboratory, was supported by Contract No. DE-AC02-06CH11357. We thank the beamline staff of the MR-CAT. The NMR facility at Caltech was supported by the National Science Foundation (NSF) Grant 9724240 and supported in part by the NSF MRSEC Program Award DMR-520565.

REFERENCES

(1) Francis, J.; Guillon, E.; Bats, N.; Pichon, C.; Corma, A.; Simon, L. J. *Appl. Catal., A* **2011**, *409*−*410*, 140−147.
(2) Bhatia, S. In *Zeolite Catalysts: Principles and Applications*; CRC Press: Boca Raton, FL, 1990; p 134.
(3) Azzam, K. G.; Jacobs, G.; Shafer, W. D.; Davis, B. H. *Appl. Catal., A* **2010**, *390*, 264−270.
(4) Gallezot, P. Preparation of Metal Clusters in Zeolites. In *Molecular Sieves*; Karge, H. G., Weitkamp, J., Eds.; Springer Berlin: Heidelberg, 2002; Vol. 3, pp 257−306.
(5) Maier, S. M.; Jentys, A.; Lercher, J. A. *J. Phys. Chem. C* **2011**, *115*, 8005−8013.
(6) Dwyer, J.; O'Malley, P. J. In *Keynotes in Energy-Related Catalysis*; Kaliaguine, S., Ed.; Elsevier: Amsterdam, 1988; Vol. *35*; p 28.
(7) Cairon, O.; Chevreau, T.; Lavalley, J. C. *J. Chem. Soc., Faraday Trans.* **1998**, *94*, 3039−3047.
(8) Uzun, A.; Bhirud, V. A.; Kletnieks, P. W.; Haw, J. F.; Gates, B. C. *J. Phys. Chem. C* **2007**, *111*, 15064−15073.
(9) Solymosi, F.; Novák, E.; Molnár, A. *J. Phys. Chem.* **1990**, *94*, 7250−7255.
(10) Mihaylov, M.; Ivanova, E.; Thibault-Starzyk, F.; Daturi, M.; Dimitrov, L.; Hadjiivanov, K. I. *J. Phys. Chem. B* **2006**, *10*, 10383−10389.
(11) Miessner, H.; Burkhardt, I.; Gutschick, D.; Zecchina, A.; Morterra, C.; Spoto, G. *J. Chem. Soc., Faraday Trans. 1* **1989**, *85*, 2113−2126.
(12) Ogino, I.; Gates, B. C. *J. Phys. Chem. C* **2010**, *114*, 2685−2693.
(13) Lu, J.; Serna, P.; Gates, B. C. *ACS Catal.* **2011**, *1*, 1549−1561.
(14) Parker, L. M.; Bibby, D. M.; Burns, G. R. *Zeolites* **1991**, *11*, 293−297.

(15) Lohse, U.; Löffler, E.; Hunger, M.; Stöckner, J.; Patzelová, V. *Zeolites* **1987**, *7*, 11−13.
(16) Serna, P.; Gates, B. C. *J. Catal.* **2013**, *308*, 201−212.
(17) Karge, H. G.; Hunger, M.; Beyer, H. K. In *Catalysis and Zeolites: Fundamentals and Applications*; Weitkamp, J., Puppe, L., Eds.; Springer: Berlin, 1999; p 257.
(18) Xu, R.; Pang, W.; Yu, J.; Huo, Q.; Chen, J. In *Chemistry of Zeolites and Related Porous Materials: Synthesis and Structure*; Wiley: Singapore, 2007; p 201.
(19) Ray, G. J.; Nerheim, A. G.; Donohue, J. A. *Zeolites* **1988**, *8*, 458−463.
(20) Poltorak, O. M.; Boronin, V. S. *Russ. J. Phys. Chem.* **1966**, *40*, 1436−1445.
(21) Aydin, C.; Lu, J.; Browning, N. D.; Gates, B. C. *Angew. Chem., Int. Ed.* **2012**, *51*, 5929−5934.
(22) Fierro-Gonzalez, J. C.; Hao, Y.; Gates, B. C. *J. Phys. Chem. C* **2007**, *111*, 6645−6651.

dx.doi.org/10.1021/cs5006426 | *ACS Catal.* 2014, 4, 2662−2666